Chemical Engineering Science 189 (2018) 33–42

Contents lists available at ScienceDirect

Chemical Engineering Science

journal homepage: www.elsevier.com/locate/ces

Modeling water imbibition into coated and uncoated papers

Behzad Ghanbarian [a,*], Hamed Aslannejad [b], Amir Raoof [b]

[a] Department of Geology, Kansas State University, Manhattan, KS, USA
[b] Multiscale Porous Media Lab., Department of Earth Sciences, Utrecht University, Utrecht, The Netherlands

HIGHLIGHTS

- Pore size distribution of coated/uncoated papers followed lognormal distribution.
- A critical-path-analysis model was proposed to estimate relative permeability k_{rw}.
- Comparing to simulations showed that k_{rw} was accurately estimated under imbibition.

ARTICLE INFO

Article history:
Received 10 February 2018
Received in revised form 22 May 2018
Accepted 25 May 2018
Available online 26 May 2018

Keywords:
Coated and uncoated papers
Pore scale
Critical path analysis
Imbibition
Water relative permeability
Log-normal distribution

ABSTRACT

Modeling morphological and hydraulic properties of thin porous media, such as filter layers and papers is highly relevant to various industries. In our previous studies, the X-ray tomography and FIB-SEM methods were applied to capture micro- and nano-scale pores in uncoated paper and coated layer, respectively. Here, the reconstructed pore structures were used to investigate two-phase water imbibition in these porous media. The obtained pore size distributions showed a log-normal probability density function. Such a distribution, together with concepts from critical path analysis and percolation theory, was applied to calculate relative permeability over a wide range of water saturations. Comparison with pore-scale numerical simulations showed the capability of this method to estimate water relative permeability for coated and uncoated papers.

1. Introduction

Several different industries deal with thin porous media in their production processes. These include coating layers and papers is the printing industry, food packaging, and production of filters and membranes. The morphological and hydraulic properties of such thin layers are often critical in the process performance. Advanced high-resolution computed tomography provides a minimally-destructive and direct technique to determine pore space morphological and physical properties of thin porous media. Various algorithms have been developed to generate pore structures (Raoof and Hassanizadeh, 2012) or to analyze three-dimensional images (e.g., Lindquist et al., 1996; Silin et al., 2003; Øren and Bakke, 2003) to quantify pore space geometrical and topological properties. For example, Lindquist et al. (1996) introduced the medial axis as a technique to analyze the acquired geometric structure of pore space in porous media. Delerue et al. (1999) proposed a method based on skeletization to determine the void space from 3D images. In another study, Silin et al. (2003) proposed an algorithm in which the skeleton of the pore space is captured through maximal balls associated with each voxel. Those authors used the maximal ball distribution to simulate a dimensionless drainage capillary pressure curve and showed that their method provided realistic estimates of the number and shapes of pores and throats as well as the pore coordination number. More recently, Raoof and Hassanizadeh (2012) introduced a method to numerically generate pore structures with variable coordination number up to 26 connected neighbors at each pore.

During the printing process, liquid penetration into the paper (known as imbibition process) depends on several factors and mechanisms such as geometrical and morphological properties of pores (e.g., Ghassemzadeh et al., 2001), pore size distribution (Liu et al., 2017), and pore-solid interface roughness and wetting force (Liu et al., 2014a, 2014b). For instance, Ghassemzadeh et al. (2001) developed a new imbibition model of a coating fluid in a fibrous layer. The three-dimensional pore network of paper was represented by the interconnection of flow channels between fibers. Ghassemzadeh et al. (2001) found that the mean coordination number (i.e., the interconnectivity of the channels) and the average

* Corresponding author.
E-mail address: ghanbarian@ksu.edu (B. Ghanbarian).

https://doi.org/10.1016/j.ces.2018.05.051
0009-2509/

pore size of the paper strongly influenced imbibition of the coating fluid. Using a high-speed camera, Koivula et al. (2012) studied the influence of coating surface structure and pre-saturation state on the spreading of liquid. Results showed a high impact of pigment-based structure on the liquid distribution in both dry and pre-saturated structures. However, under the pre-saturated conditions, liquid-liquid interactions were the controlling mechanism. Koivula et al. (2012) showed the effectiveness of nano-size pores located in a calcium carbonate comprising base layer to increase capillarity absorption. In another study, Lamminmäki et al. (2011) investigated a set of critical parameters for print durability. In coated inkjet papers, the surface is treated based on pore-network of layer and addition of polymer binders to produce good ink fastness properties. Based on their study, low permeability of coating layer and bounding colorant part of ink by charge interactions could produce required print quality.

Pore-scale imaging has become a promising method to study fluid flow and transport in porous materials (see e.g., Raoof et al., 2013; Liu and Mostaghimi, 2017). Although there exist some challenges such as identifying a representative elementary volume (REV), needed to define macroscopic properties, and the resolution effect, there has been significant progress in three-dimensional imaging, especially in thin porous media. For instance, Huang et al. (2002) proposed a method based on X-ray micro-tomography imaging and determined porosity, pore size distribution, and specific surface area for fibers. Their results agreed reasonably well with the measured values using the mercury intrusion porosimetry method. More recent developments in pore-scale tomographic imaging of porous media can be found at Wildenschild and Sheppard (2013).

Pore-network models have also been used to study fluid flow in thin porous media. For example, Ghassemzadeh and Sahimi (2004a) carried out extensive computational simulations to investigate the effect of the microstructure of paper's pore space on the effective permeability tensor. They concluded that the distribution of fibers and consequently coordination number has a strong impact on fluid flow properties in fibrous layers. In another study, Ghassemzadeh and Sahimi (2004b) simulated the imbibition process of a coating fluid into a paper using a network of interconnected channels. Their results showed that the connectivity of the channels, the anisotropic structure of the paper's pore space, and the dynamic pressure distribution had strong effects on the imbibition process.

In the literature, various theoretical approaches have been used to model water relative permeability in porous media. Some models were developed based on the parallel (e.g., Purcell, 1949; Burdine, 1953), series-parallel (e.g., Mualem, 1976; Kosugi, 1999), or tortuous parallel (e.g., Zheng et al., 2013; Zhang et al., 2017) capillary tubes approach. However, such models are distorted idealizations (Sahimi, 2011; Hunt et al., 2014), since pores in porous media exist neither in series nor in parallel, but are distributed throughout an interconnected and complex multi-scale network.

In addition to the bundle of capillary tubes model, effective-medium theory has been utilized to estimate the relative permeability k_r (see e.g., Petropoulos et al., 1989; Kainourgiakis et al., 1998; Ghanbarian et al., 2016a). For example, Ghanbarian et al. (2016a) assumed that the pore size distribution of porous media followed a power-law form and determined its parameters (including pore space fractal dimension) from the capillary pressure curve. Invoking Kirkpatrick's effective-medium theory, Ghanbarian et al. (2016a) estimated the relative permeability for water, k_{rw}, from measured capillary pressure data and found good agreement with experiments. However, those authors reported k_{rw} underestimations via effective-medium theory in porous media with broad pore size distribution.

Hunt (2001) was probably the first to apply concepts from critical path analysis (CPA) to model k_{rw} in porous media with broad hydraulic conductance (or pore size) distribution. Hunt (2001) combined CPA with the power-law pore size distribution whose parameters were determined from the capillary pressure curve. By comparison with experiments, Hunt (2001) showed that CPA accurately estimated k_{rw}, particularly at high water saturations. Years later, Ghanbarian-Alavijeh and Hunt (2012) combined CPA with the pore-solid fractal model and proposed a more general water relative permeability relationship. Results of Ghanbarian-Alavijeh and Hunt (2012), Ghanbarian et al. (2015a, 2016b), and Ghanbarian and Hunt (2017) indicated that the proposed general model estimated k_{rw} accurately.

Concepts from CPA and power-law pore size distribution have been applied to estimate k_{rw} from the measured capillary pressure curve. However, to the best of the authors' knowledge CPA has never been combined with the log-normal pore size distribution to predict k_{rw}. Nor has it been used to estimate k_{rw} directly from the pore size distribution and three-dimensional reconstructed pore structure derived from FIB-SEM imaging. Therefore, the main objectives of this study are: (1) to develop a theoretical k_{rw} model based on CPA and log-normal pore size distribution, and (2) to evaluate the proposed approach in the estimation of k_{rw} from measured pore size distribution for thin porous media like paper coating layers and uncoated papers.

2. Theory

2.1. Pore size distribution and capillary pressure curve

Thin porous media such as fibrous layers consist of solid matrix and pore space. The latter is formed of void regions of irregular shapes and various sizes spanning orders of magnitude from several nanometers to a few hundred micrometers. Similar to natural porous media such as rocks and soils, the geometrical definition of a single pore is ambiguous in fibrous layers and papers. This, accordingly, makes determination of the actual distribution of pore sizes difficult. Nonetheless, following Qin and Hassanizadeh (2014) and Qin et al. (2016), we assume that pore sizes in thin porous media conform to the following truncated log-normal probability density function $f(r)$

$$f(r) = \frac{A}{\sqrt{2\pi}\sigma r}\exp\left[-\left(\frac{\ln\left(\frac{r}{r_m}\right)}{\sqrt{2}\sigma}\right)^2\right],\quad r_{min} \leqslant r \leqslant r_{max} \tag{1}$$

in which,

$$A = \frac{2}{\mathrm{erf}\left(\frac{\ln\left(\frac{r_{max}}{r_m}\right)}{\sqrt{2}\sigma}\right) - \mathrm{erf}\left(\frac{\ln\left(\frac{r_{min}}{r_m}\right)}{\sqrt{2}\sigma}\right)} \tag{2}$$

where erf is the error function, r is the pore radius, r_{min} and r_{max} are the smallest and largest pore radii, respectively, representing the lower and upper bounds of the log-normal distribution, r_m is the geometric mean pore radius, and σ is the log-normal standard deviation. The value of r_m, r_{min}, r_{max}, and σ can be determined by directly fitting Eq. (1) to the pore size distribution derived from, e.g., tomography images.

Following Eq. (1), the porosity ϕ of the medium is

$$\begin{aligned}\phi &= \int_{r_{min}}^{r_{max}} sr^3 f(r)\mathrm{d}r + \theta_r \\ &= \frac{sAr_m^3}{2}\exp\left(\frac{9\sigma^2}{2}\right)\left[\mathrm{erf}\left(\frac{3\sigma^2 - \ln\left(\frac{r_{min}}{r_m}\right)}{\sqrt{2}\sigma}\right) - \mathrm{erf}\left(\frac{3\sigma^2 - \ln\left(\frac{r_{max}}{r_m}\right)}{\sqrt{2}\sigma}\right)\right] + \theta_r\end{aligned} \tag{3}$$

where s is a pore shape factor, θ_r is residual water content, which is formed from water existing in some subset of the pores in the range [r_{min}, r_{max}] but may also reflect water in pore spaces existing at scales less than r_{min}. Note that when ϕ, r_{min}, r_{max}, r_m, σ, and θ_r are known, one can determine the average value of the pore shape factor s from Eq. (3).

In accordance with Eq. (3), the volumetric water content θ is defined as

$$\theta = \int_{r_{min}}^{r} sr^3 f(r)\mathrm{d}r + \theta_r = \frac{sAr_m^3}{2}\exp\left(\frac{9\sigma^2}{2}\right)\left[\mathrm{erf}\left(\frac{3\sigma^2 - \ln\left(\frac{r_{min}}{r_m}\right)}{\sqrt{2}\sigma}\right) - \mathrm{erf}\left(\frac{3\sigma^2 - \ln\left(\frac{r}{r_m}\right)}{\sqrt{2}\sigma}\right)\right] + \theta_r \quad (4)$$

In Eq. (4), it is also assumed that each pore of the porous medium is occupied by either water or air. Integrating over pores between r_{min} and r necessarily means that all pores with size r and greater are accessible to air and, hence, collectively drained.

The relationship between water saturation and pore radius is derived by combining Eqs. (3) and (4) as follows:

$$S_e = \frac{\mathrm{erf}\left(\frac{3\sigma^2 - \ln\left(\frac{r_{min}}{r_m}\right)}{\sqrt{2}\sigma}\right) - \mathrm{erf}\left(\frac{3\sigma^2 - \ln\left(\frac{r}{r_m}\right)}{\sqrt{2}\sigma}\right)}{\mathrm{erf}\left(\frac{3\sigma^2 - \ln\left(\frac{r_{min}}{r_m}\right)}{\sqrt{2}\sigma}\right) - \mathrm{erf}\left(\frac{3\sigma^2 - \ln\left(\frac{r_{max}}{r_m}\right)}{\sqrt{2}\sigma}\right)}, \quad r_{min} \leqslant r \leqslant r_{max} \quad (5)$$

where the effective water saturation $S_e = (S_w - S_{wr})/(S_{wmax} - S_{wr})$ in which S_w is the water saturation ($=\theta/\phi$), S_{wr} is the residual water saturation, and S_{wmax} is the maximum water saturation corresponding to fully saturated conditions on the capillary pressure curve.

Combining Eq. (5) with the *Young-Laplace* equation ($P = 2\gamma\cos(\omega)/r$, where P is the capillary pressure, γ is the interfacial tension and ω is the contact angle) provides the following mathematical formula describing the effective saturation in terms of the capillary pressure for log-normally distributed pore sizes:

$$S_e = \frac{\mathrm{erf}\left(\frac{3\sigma^2 - \ln\left(\frac{P_m}{P_{max}}\right)}{\sqrt{2}\sigma}\right) - \mathrm{erf}\left(\frac{3\sigma^2 - \ln\left(\frac{P_m}{P}\right)}{\sqrt{2}\sigma}\right)}{\mathrm{erf}\left(\frac{3\sigma^2 - \ln\left(\frac{P_m}{P_{max}}\right)}{\sqrt{2}\sigma}\right) - \mathrm{erf}\left(\frac{3\sigma^2 - \ln\left(\frac{P_m}{P_{min}}\right)}{\sqrt{2}\sigma}\right)}, \quad P_{min} \leqslant P \leqslant P_{max} \quad (6)$$

where P_m is the pressure ($=2\gamma\cos(\omega)/r_m$) corresponding to the geometric mean pore radius (r_m), and P_{min} and P_{max} are the minimum and maximum capillary pressures, respectively ($=2\gamma\cos(\omega)/r_{max}$ and $2\gamma\cos(\omega)/r_{min}$).

2.2. Modeling water relative permeability using critical path analysis and percolation theory

Critical path analysis (CPA) was introduced by Ambegaokar et al. (1971) and Pollak (1972). It is a promising analytical approach to estimate permeability in inhomogeneous porous media with broad pore size distribution (Katz and Thompson, 1986; Hunt, 2001). Based on CPA, transport in an uncorrelated heterogeneous network of pores is controlled by those with magnitudes that are greater than some critical pore size. The critical pore radius r_c is defined as the smallest pore such that the set of pores with $r > r_c$ forms a conducting sample-spanning cluster (Katz and Thompson, 1987).

By invoking concepts from CPA and assuming a log-normal pore size distribution (Eq. (1)), one may define the critical water saturation for water permeability, S_{wc}, under fully saturated conditions as follows:

$$S_{wc} = \frac{1}{\phi}\int_{r_c(S_w=1)}^{r_{max}} sr^3 f(r)\mathrm{d}r + S_{wr} = \frac{sAr_m^3}{2\phi}\exp\left(\frac{9\sigma^2}{2}\right)\left[\mathrm{erf}\left(\frac{3\sigma^2 - \ln\left(\frac{r_c(S_w=1)}{r_m}\right)}{\sqrt{2}\sigma}\right) - \mathrm{erf}\left(\frac{3\sigma^2 - \ln\left(\frac{r_{max}}{r_m}\right)}{\sqrt{2}\sigma}\right)\right] + S_{wr} \quad (7)$$

Note that $S_{wc} = S_{wr}$, if $r_c(S_w = 1) = r_{max}$. In accordance with Eqs. (3) and (4), in Eq. (7) we assume that water existing in some subset of the pores in the range of r_{min} and r_{max} as well as water in pore spaces present at scales smaller than r_{min} do not effectively contribute to fluid flow and accordingly to water relative permeability.

Under partially saturated conditions we have

$$S_{wc} = \frac{1}{\phi}\int_{r_c(S_w)}^{r} sr^3 f(r)\mathrm{d}r + S_{wr} = \frac{sAr_m^3}{2\phi}\exp\left(\frac{9\sigma^2}{2}\right)\left[\mathrm{erf}\left(\frac{3\sigma^2 - ln\left(\frac{r_c(S_w)}{r_m}\right)}{\sqrt{2}\sigma}\right) - \mathrm{erf}\left(\frac{3\sigma^2 - \ln\left(\frac{r}{r_m}\right)}{\sqrt{2}\sigma}\right)\right] + S_{wr} \quad (8)$$

Rewriting Eqs. (7) and (8) gives,

$$r_c(S_w = 1) = r_m \exp\left[3\sigma^2 - \sqrt{2\sigma^2}\mathrm{erf}^{-1}\left(\frac{\phi(S_{wc} - S_{wr})}{C} + \mathrm{erf}\left(\frac{3\sigma^2 - \ln\left(\frac{r_{max}}{r_m}\right)}{\sqrt{2}\sigma}\right)\right)\right] \quad (9)$$

$$r_c(S_w) = r_m \times \exp\left[3\sigma^2 - \sqrt{2\sigma^2}\mathrm{erf}^{-1}\left(\frac{\phi(S_{wc} - S_{wr})}{C} + \mathrm{erf}\left(\frac{3\sigma^2 - \ln\left(\frac{r}{r_m}\right)}{\sqrt{2}\sigma}\right)\right)\right] \quad (10)$$

in which $C = \frac{sAr_m^3}{2}\exp\left(\frac{9\sigma^2}{2}\right)$.

Within the critical path analysis framework, the water permeability k_w is proportional to the critical hydraulic conductance i.e., $k_w \propto g_c$ (Hunt, 2001; Ghanbarian-Alavijeh and Hunt, 2012). Therefore, the relative water permeability k_{rw} can be defined as

$$k_{rw} = \frac{k_w(S_w)}{k_w(S_w = 1)} = \frac{g_c(S_w)}{g_c(S_w = 1)} = \left(\frac{r_c(S_w)}{r_c(S_w = 1)}\right)^{\alpha} = \left[\frac{\exp\left(3\sigma^2 - \sqrt{2\sigma^2}\mathrm{erf}^{-1}\left(\frac{\phi(S_{wc} - S_{wr})}{C} + \mathrm{erf}\left(\frac{3\sigma^2 - \ln\left(\frac{r}{r_m}\right)}{\sqrt{2}\sigma}\right)\right)\right)}{\exp\left(3\sigma^2 - \sqrt{2\sigma^2}\mathrm{erf}^{-1}\left(\frac{\phi(S_{wc} - S_{wr})}{C} + \mathrm{erf}\left(\frac{3\sigma^2 - \ln\left(\frac{r_{max}}{r_m}\right)}{\sqrt{2}\sigma}\right)\right)\right)}\right]^{\alpha} \quad (11)$$

where $k_w(S_w)$ and $k_w(S_w = 1)$ are water permeabilities under partially and fully saturated conditions, respectively, and α is the exponent in Poiseuille's law i.e., $g \propto r^{\alpha}$ whose value is equal to 4. Note that Eq. (11) describes k_{rw} in terms of pore radius r, not water saturation S_w. However, one may relate r to S_w via Eq. (5).

Based on concepts from percolation theory, above but near the critical water saturation S_{wc} the water relative permeability should conform to the following universal power law

$$k_{rw} = k_0(S_w - S_{wc})^t, \quad S_w > S_{wc} \quad (12)$$

where k_0 is a constant coefficient. The exponent t in Eq. (12) is universal, and its value only depends on the dimensionality of the system; $t = 1.3$ in two and $t = 2$ in three dimensions (Stauffer and Aharony, 1994).

We, accordingly, use CPA (Eq. (11)) for estimating k_{rw} at high to intermediate water saturations, and apply the universal power law (Eq. (12)) to determine k_{rw} at low S_w values near the critical water saturation S_{wc}. The crossover between the two occurs at some water saturation S_{wx} (or effective water saturation S_{ex}).

3. Materials and methods

In this section, we describe images analysis and pore-scale numerical simulations. Then, we present how one can estimate the water relative permeability from the pore size distribution derived from FIB-SEM images and micro-CT tomography. We present the imbibition water relative permeability estimates from the pore size distribution for one paper coating layer and one uncoated paper. The former is mainly made of calcium carbonate grains, while the latter is a fibrous layer out of cellulose fibers.

3.1. Paper coating layer

Due to the presence of nano-size pores (often in the range of 10–600 nm) in the coating layer of papers, Aslannejad et al. (2017) utilized the Focused Ion Beam Scanning Electron Microscopy (FIB-SEM) technique to image the structure of the coating layer's pore space at the nano scale. The domain of interest was about $10 \times 10 \times 10\ \mu m^3$, and imaging was carried out with the very high resolution of 3 nm. The resulting stack of 2D images was then aligned and segmented to reconstruct a 3D domain (see Fig. 1). The pore network was then analyzed using Avizo 9.1 in order to determine the volume of pores, porosity value (see Table 1), and pore size distribution of the sample (see Fig. 3). The solid-liquid contact angle was assumed to be 45° (Järnström et al., 2010). Based on porosity and permeability simulations for different domain sizes, Aslannejad et al. (2017) showed that the representative elementary volume (REV) of the paper coating layer was around $4 \times 4 \times 4\ \mu m^3$, which provides the smallest domain size for accurate representative values of the layer hydraulic properties. The determined REV size was then used to calculate capillary pressures corresponding to certain saturation levels using the pore-morphology method available in the Geo-Dict software (Math2Market, Kaiserslautern, Germany). Accordingly, the primary imbibition and drainage curves were simulated. Solving the Stokes equation for both wetting and non-wetting phases under various saturation degrees provided permeability and relative permeability values.

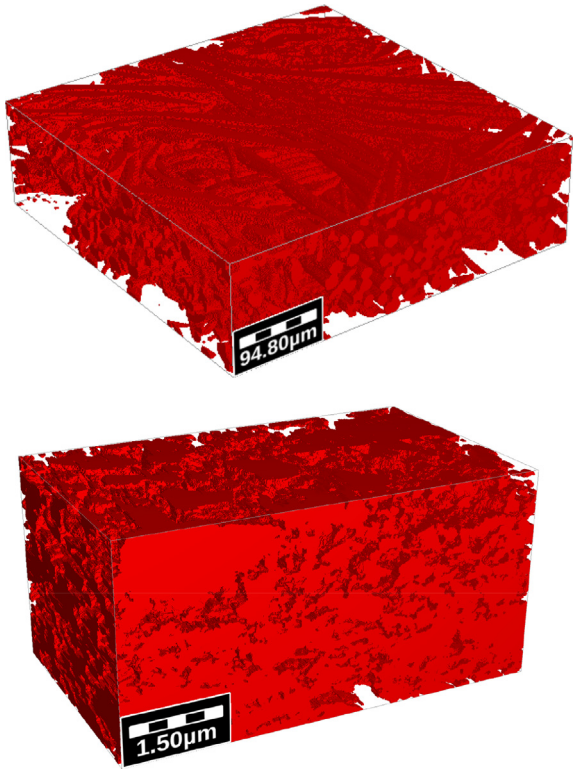

Fig. 1. Three-dimensional reconstructed domains of the uncoated paper (top) and the paper coating layer (bottom) studied here. The red colors indicate the binarized solid phases. (For interpretation of the references to color in this figure legend, the reader is referred to the web version of this article.)

3.2. Uncoated paper

Compared to coated layers, uncoated papers are typically composed of significantly larger pores in the range of 1–40 μm. Therefore, Aslannejad and Hassanizadeh (2017) used micro-CT imaging to study fluid flow through the pore space of an uncoated paper. Using image analysis methods, the three-dimensional structure of the paper was reconstructed (see Fig. 1) and further used to determine its porosity and pore size distribution. Aslannejad and Hassanizadeh (2017) found that the REV size of the uncoated paper was $400 \times 400 \times 150\ \mu m^3$ by computing porosity and permeability values as well as capillary pressure curves at various domain sizes. This size is significantly greater than the REV size that Aslannejad et al. (2017) found for the paper coating layer composed of much smaller pores. The porosity of the sample was determined from image analysis and found to be 0.5. The solid-liquid contact angle for the uncoated paper was assumed to be 15° (Liukkonen, 1997; Aslannejad and Hassanizadeh, 2017). This value was experimentally measured in the lab (results not published yet). Using the pore-morphology method, Aslannejad and Hassanizadeh (2017) numerically simulated the imbibition and drainage capillary pressure curves (see their Figs. 7 and 8) as well as the imbibition water relative permeability (their Fig. 6) for the three-dimensional reconstructed uncoated paper.

3.3. Estimating k_{rw} from pore size distribution

To estimate the imbibition water relative permeability from the pore size distribution using Eqs. (11) and (12), one needs to determine the truncated log-normal probability density function (Eq. (1)) parameters r_{min}, r_m, r_{max}, and σ as well as ϕ, S_{wr} and S_{wc}. We directly fit Eq. (1) to the pore size distribution derived from images for both the paper coating layer and uncoated paper. A value of residual water saturation equal to zero ($S_{wr} = 0$) was determined from the numerically simulated imbibition capillary pressure curve shown in Fig. 4a for the paper coating layer and Fig. 7a for the uncoated paper. We also set $S_{wc} = 0$ for both the paper coating layer and uncoated paper. This approximation seems reasonable for the paper coating layer based on the effective porosity calculation by Aslannejad et al. (2017). Those authors found that 99.7% of

Table 1
Salient properties of the two porous media studied here.

Porous medium	r_{min} (nm)	r_{max} (nm)	r_m (nm)	σ	ϕ	S_{wr}	S_{wc}
Paper coating layer	0	500	106.6	0.534	0.34	0	0
Uncoated paper	0	80	8.5	0.733	0.50	0	0

r_{min}: minimum pore radius, r_{max}: maximum pore radius, r_m: geometric mean pore radius, σ: standard deviation of the log-normal pore size distribution, ϕ: porosity, S_{wr}: residual water saturation, and S_{wc}: critical water saturation.

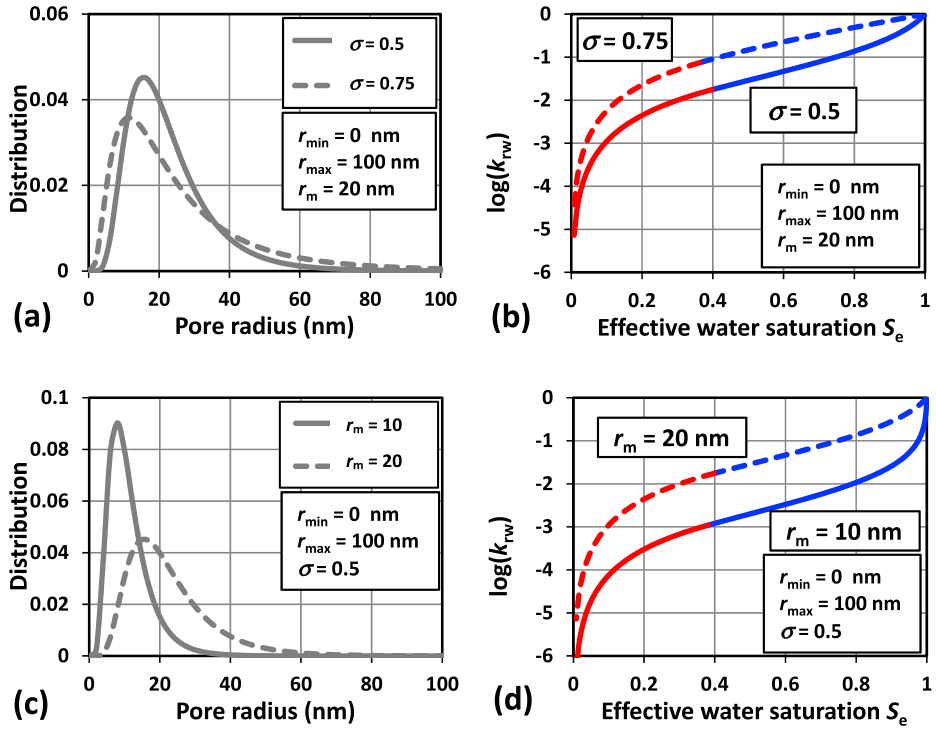

Fig. 2. Log-normal pore size distributions (left plots – a and c) and corresponding water relative permeability curves (right plots – b and d) for different values of the statistical parameters. The blue and red lines represent the results of critical path analysis (Eq. (11)) and universal power-law scaling from percolation theory (Eq. (12)), respectively.

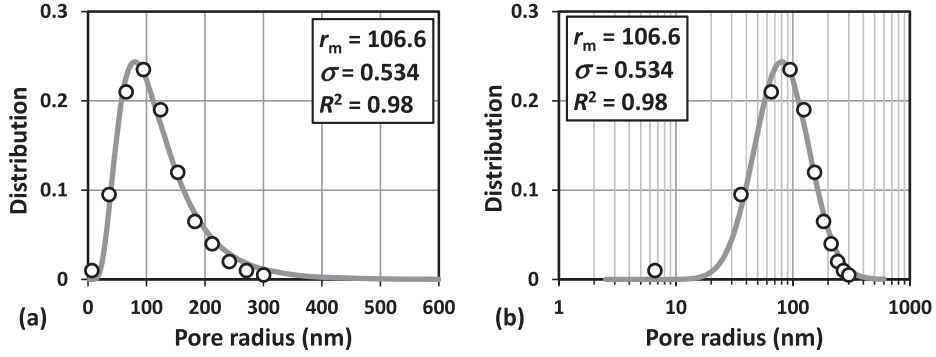

Fig. 3. The paper coating layer pore size distribution derived from FIB-SEM tomography on (a) natural scale and (b) semilog scale. The gray line represents the log-normal distribution fitted to the data. We found r_{min} = 0 nm, r_{max} = 500 nm, r_m = 106.6 nm, σ = 0.534 and R^2 = 0.98. Circles denote data from Aslannejad et al. (2017).

pores in the paper coating layer were connected (effective porosity of 0.339 vs. total porosity of 0.34; see their Table 1). However, taking S_{wc} = 0 might be less accurate for the uncoated paper, as we discuss in Section 4.3. The salient properties of both paper coating layer and uncoated paper are presented in Table 1.

We determined k_0 by setting Eqs. (11) and (12) equal at the crossover water saturation S_{wx}. The value of S_{wx} can be computed by setting the first derivative of the two equations equal. For the sake of simplicity, we calculated k_0 and the S_{wx} values numerically. More specifically, using the spline function we interpolated values of k_{rw} from Eq. (11) at various water saturations between S_{wc} and 1. We then calculated k_0 and determined the slope at each water saturation numerically. The crossover point is the water saturation at which the slope of Eq. (11) is equal to that of Eq. (12). Accordingly, to estimate k_{rw} over the entire range of water saturation, we applied Eq. (11) for $S_{wx} \le S_w \le 1$, and Eq. (12) for $S_{wc} \le S_w \le S_{wx}$. Note that since the REV domain for both paper coating layer and uncoated paper is three-dimensional, we set t = 2 in Eq. (12).

4. Results

Here, we first present results of the sensitivity of our water relative permeability model to two input parameters σ and r_m. We then compare theoretical estimates of k_{rw} with numerical simulations for the paper coating layer and the uncoated paper.

4.1. Sensitivity analysis

To study the sensitivity of the proposed k_{rw} model to parameters σ and r_m, we considered a porous medium with ϕ = 0.35, r_{min} = 0 nm, r_{max} = 100 nm, S_{wr} = 0, and S_{wc} = 0. We then used different values of standard deviation, σ = 0.5 and 0.75, and the geometric mean pore radius, r_m = 10 and 20 nm, to determine k_{rw} as a function of the effective water saturation, S_e. Fig. 2 shows the log-normal pore size distributions together with their corresponding k_{rw}-S_e curves where the blue and red lines represent the CPA

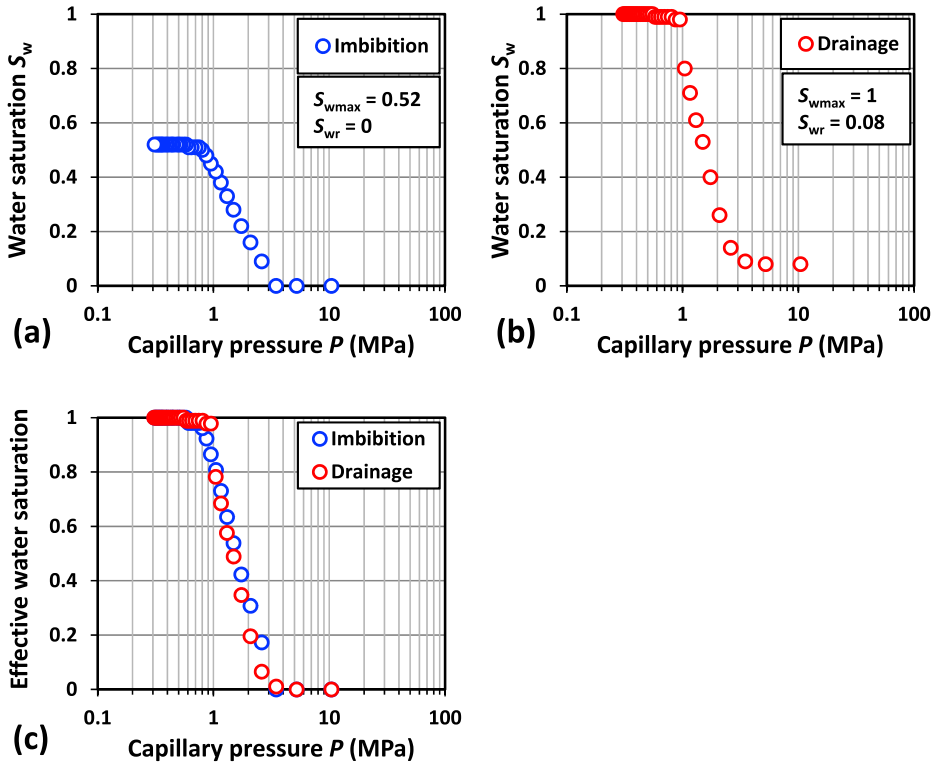

Fig. 4. The pore-scale numerically-simulated capillary pressure curve under (a) imbibition and (b) drainage conditions for the paper coating layer. (c) The effective water saturation $S_e = (S_w - S_{wr})/(S_{wmax} - S_{wr})$ against the capillary pressure for both imbibition and drainage curves. Circles denote the numerically-simulated data from Aslannejad et al. (2017).

estimates (Eq. (11)) and those by the universal power law from percolation theory (Eq. (12)), respectively. In Fig. 2a, we set r_m = 20 nm but changed σ from 0.5 to 0.75. As can be seen, the pore size distribution with σ = 0.75 has slightly a higher number of larger pores (e.g., 40 < r < 100 nm) than that with σ = 0.5, which caused the former to have a greater relative permeability compared to the latter (see Fig. 2b).

Fig. 2c shows two pore size distributions with the same standard deviation (σ = 0.5) but different geometric mean pore radii (r_m = 10 and 20 nm). Similar to Fig. 2a, the frequency of larger pores for the pore size distribution with r_m = 20 nm is greater than that for the pore size distribution with r_m = 10 nm. Accordingly, one should expect k_{rw} corresponding to r_m = 20 nm to be greater than that corresponding to r_m = 10 nm (see Fig. 2d). Unlike the power-law pore size distribution (see e.g., Fig. 1 of Ghanbarian et al. (2016b)), the heavy tail of the log-normal pore size distribution at large pore radius scales causes a sharp reduction in k_{rw} at saturations near 1 and accordingly a sigmoidal shape of k_{rw}, as shown in Fig. 2d. Fig. 2 also indicates that overestimating σ or r_m results in the overestimation of k_{rw}. Furthermore, the region of applicability of CPA does not change remarkably as σ and r_m varied by 50% and 100%, respectively.

4.2. K_{rw} estimation for the paper coating layer

The pore size distribution of the paper coating layer is presented in Fig. 3. As shown, the log-normal distribution, Eq. (1), with r_{min} = 0 nm, r_{max} = 500 nm, r_m = 106.6 nm and σ = 0.534 is well fitted to the data (R^2 = 0.98). Fig. 4 presents the simulated capillary pressure curve under imbibition (Fig. 4a) and drainage (Fig. 4b) conditions. Results show that S_{wmax} = 0.52 and S_{wr} = 0 for the imbibition curve and S_{wmax} = 1 and S_{wr} = 0.08 for the drainage. Although the imbibition capillary pressure curve (Fig. 4a) appears different from the drainage one (Fig. 4b), using the effective water saturation S_e the two capillary pressure curves interestingly collapsed into a single curve (see Fig. 4c). This suggests that the effect of hysteresis should be negligible.

The estimated and simulated imbibition water relative permeability k_{rw} as a function of effective water saturation S_e are presented in Fig. 5 for the paper coating layer. As can be observed, the proposed water relative permeability model (Eqs. (11) and (12)) was able to accurately estimate k_{rw} from the measured pore size distribution over the entire range of effective water saturation. We found the crossover effective water saturation S_{ex} = 0.38 above which the CPA accurately characterized k_{rw} (shown in blue) and below which the universal power-law scaling from percolation theory precisely estimated k_{rw} (shown in red).

Aslannejad et al. (2017) applied the van Genuchten-Mualem model (Mualem, 1976; van Genuchten, 1980) and estimated k_{rw} from the simulated imbibition capillary pressure curve shown in Fig. 4a. Those authors found that the *van Genuchten-Mualem* model overestimated k_{rw} somewhat at higher S_e values (see their Fig. 9). Our approach (i.e., Eqs. (11) and (12)) apparently estimated k_{rw} from the pore size distribution more accurately. However, it slightly underestimated k_{rw} at higher S_e values (see Fig. 5).

The *van Genuchten-Mualem* model was developed on the basis of the series-parallel capillary tubes approach, while our model is based on randomly distributed pores in a porous medium with a broad pore size distribution. Another difference between the two model is that in the *van Genuchten-Mualem* model the critical water saturation for water relative permeability is typically assumed to be equal to the residual water saturation estimated from the capillary pressure curve, while our model differentiates between S_{wc} and S_{wr} (see Eqs. (7) and (8)), similar to the model of Ghanbarian et al. (2017). However, S_{wc} could be equal to S_{wr}, when $r_c(S_w = 1) = r_{max}$ or $r_c(S_w) = r_{max}$. In addition, our approach

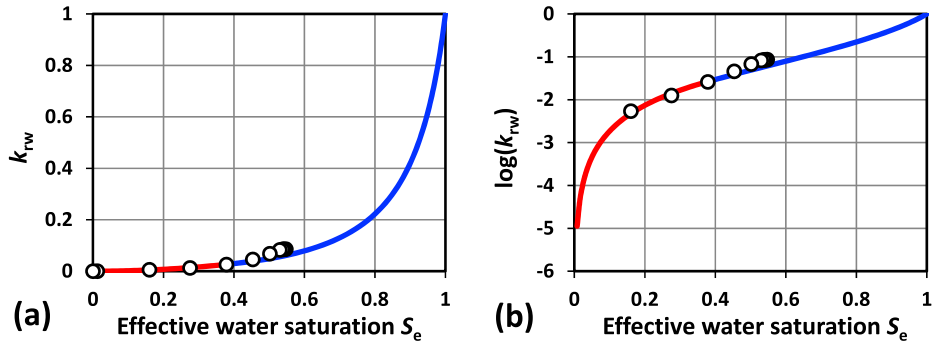

Fig. 5. (a) Estimated imbibition water relative permeability, k_{rw}, and (b) estimated logarithm of k_{rw} of the paper coating layer as a function of effective water saturation, S_e, using r_{min} = 0 nm, r_{max} = 500 nm, r_m = 106.6 nm, σ = 0.534, S_{wr} = 0, S_{wc} = 0, and α = 4. The blue and red lines represent the critical path analysis scaling (Eq. (11)) and the universal scaling from percolation theory (Eq. (12)), respectively, with the crossover effective water saturation S_{ex} = 0.38. Circles denote the numerically-simulated data from Aslannejad et al. (2017). (For interpretation of the references to color in this figure legend, the reader is referred to the web version of this article.)

estimates k_{rw} directly from pore size distribution, whereas the *van Genuchten-Mualem* model predicts k_{rw} from the capillary pressure curve. However, our model requires knowledge of residual water saturation, which can be determined from capillary pressure curve or from nuclear magnetic resonance imaging (Coates et al., 1999).

4.3. K_{rw} estimation for the uncoated paper

The pore sizes of the uncoated paper, which are considerably larger compared to the pore sizes of the coating paper, were derived using micro-CT scanning (Fig. 6). We found that the log-normal distribution, provided by Eq. (1), with r_{min} = 0 μm, r_{max} = 80 μm, r_m = 8.5 μm, σ = 0.733 could well represent the pore size distribution (R^2 = 0.93), although the data are somewhat scattered. Remarkably, the geometric mean pore radius r_m = 8.5 μm is very close to those values reported by Dodson and Sampson (1996) for diverse types of papers (see their Table 1).

The simulated imbibition and drainage capillary pressure curves are shown in Fig. 7. The maximum and residual water saturations were 0.8 and 0 for the imbibition and 1 and 0.05 for the drainage, respectively. Similar to the paper coating layer, the uncoated paper has greater S_{wmax} and larger S_{wr} values under the drainage than the imbibition (see Fig. 7). When we plotted the effective saturation, S_e, against the capillary pressure for both drainage and imbibition processes, the two capillary pressure curves collapsed into one curve (see Fig. 7c). As we stated earlier, this indicates that the hysteretic effect in such a porous medium should be trivial.

Fig. 8 shows both k_{rw} and log(k_{rw}) estimated via Eqs. (11) and (12) as well as those simulated numerically using the real 3D images along different principal directions versus S_e for the uncoated paper. We found that Eqs. (11) and (12) with r_{min} = 0 μm, r_{max} = 80 μm, r_m = 8.5 μm, σ = 0.733, S_{wr} = 0, S_{wc} = 0, S_{ex} = 0.22, and α = 4 estimated k_{rw} accurately over the whole range of the effective water saturation (see Fig. 8b). However, our theoretical model slightly underestimated k_{rw} at higher water saturations and somewhat overestimated its value at the lower saturation degrees under imbibition conditions. The latter might be related to the rough approximation of S_{wc}. The number of simulated data points at low water saturations is restricted (see Fig. 8b), and the simulations correspond to water saturations between 0.11 and 1. Nonetheless, from Fig. 8b, it can be deduced that the critical water saturation for the imbibition water relative permeability might be slightly greater than zero, the value assumed in our analyses (S_{wc} = 0). We discuss the effect of critical water saturation on water relative permeability in the next section.

5. Discussion

The CPA approach applied here is generally applicable to porous media characterized by a broad pore size distribution with only short-range correlations (Katz and Thompson, 1987). Sahimi (2011) stated that natural porous media are not necessarily random and may exhibit some correlation. For example, although packing of particles may contain only short-range correlations, heterogeneous field-scale porous media may be long-range correlated. Random and short-range correlation mean that heterogeneities in one region are random and uncorrelated with those in other regions. Furthermore, heterogeneities occur at length scales much smaller than the linear size of a porous medium. In contrast, long-range correlation means heterogeneities at various regions are correlated and correlations are often present at all the length scales (Sahimi, 2011).

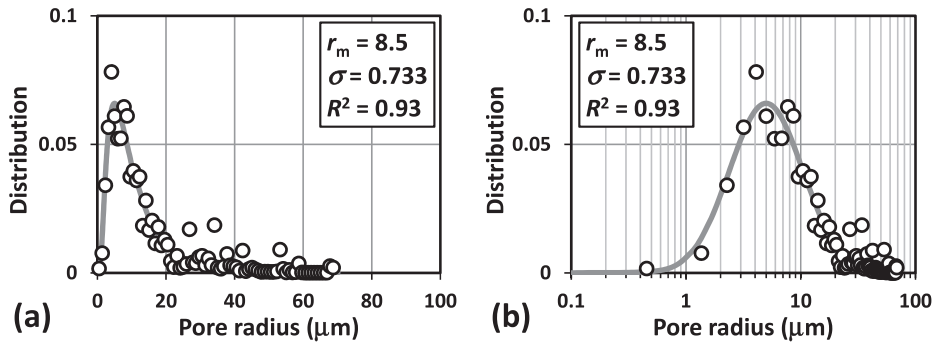

Fig. 6. The uncoated paper pore size distribution derived from 3D X-ray tomography on (a) natural scale and (b) semilog scale. The gray line represents the log-normal distribution fitted to the data. We found r_{min} = 0 μm, r_{max} = 80 μm, r_m = 8.5 μm, σ = 0.733 and R^2 = 0.93. Circles denote data from Aslannejad and Hassanizadeh (2017).

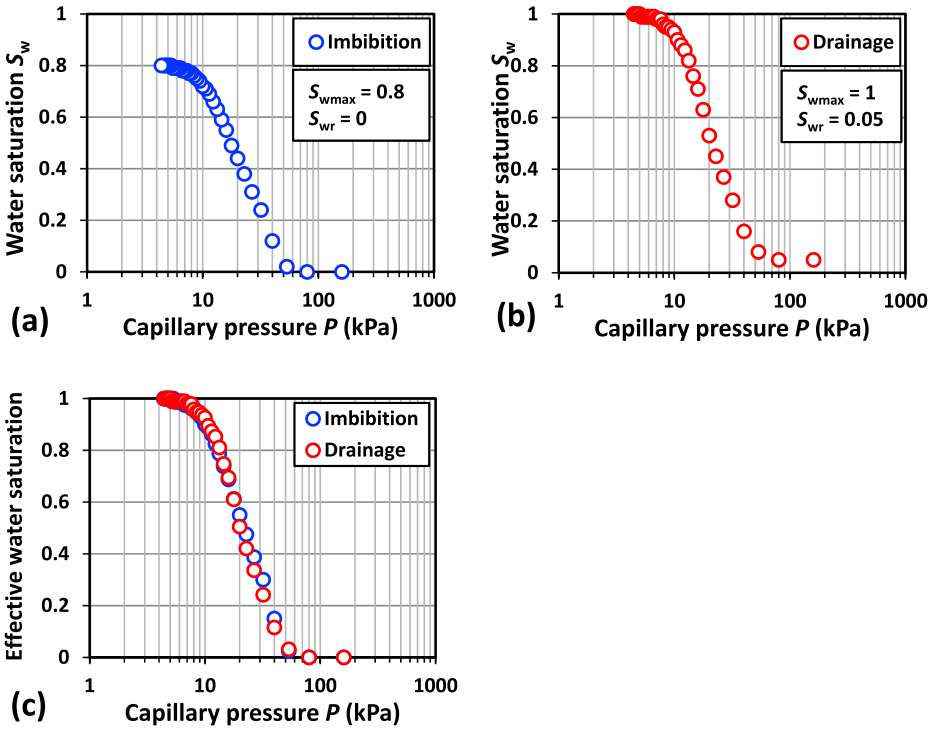

Fig. 7. The pore-scale numerically-simulated capillary pressure curve under (a) imbibition and (b) drainage conditions for the uncoated paper. (c) The effective water saturation $S_e = (S_w - S_{wr})/(S_{wmax} - S_{wr})$ against the capillary pressure for both imbibition and drainage curves. Circles denote the numerically-simulated data from Aslannejad and Hassanizadeh (2017).

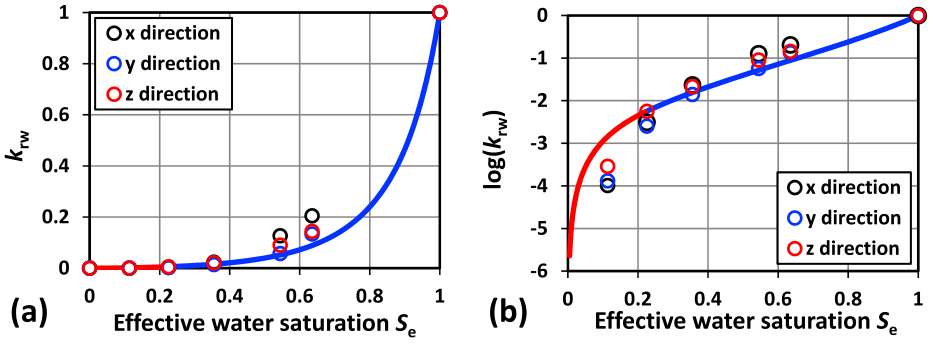

Fig. 8. (a) Estimated imbibition water relative permeability, k_{rw}, and (b) estimated logarithm of k_{rw} of the uncoated paper as a function of effective water saturation, S_e, using r_{min} = 0 μm, r_{max} = 80 μm, r_m = 8.5 μm, σ = 0.733, S_{wr} = 0, S_{wc} = 0, and α = 4. The blue and red lines represent the critical path analysis scaling (Eq. (11)) and the universal scaling from percolation theory (Eq. (12)), respectively, with the crossover effective water saturation S_{ex} = 0.22. Circles denote the pore-scale numerically-simulated data along different directions from Aslannejad and Hassanizadeh (2017). (For interpretation of the references to color in this figure legend, the reader is referred to the web version of this article.)

Critical path analysis should work accurately in random and uncorrelated porous media. Tsakiroglou and Ioannidis (2008) investigated flow in spatially pore-to-pore and pore-to-throat size correlated porous media with very broad range of pore-length scales. Those authors showed that flow through the most permeable sample-spanning cluster of pores occurs, and the application of the classical CPA approach becomes questionable. Results of Hunt and Idriss (2009), however, indicated that CPA might provide reasonably accurate permeability predictions in correlated porous media. To the authors' knowledge, there exists no supporting evidence in the literature indicating how the accuracy of CPA might diminish as long-range correlation increases.

A porous medium may be considered as a network of pore bodies and throats distributed in the medium. It is well known in the literature that the capillarity is controlled by pore bodies, while the resistance to flow in response to that capillarity is dominated by pore throats. This is because in the latter drying requires passage of interfaces through throat constrictions, whereas in the former wetting requires pore bodies to be filled (see e.g., Sahimi, 1994; Hunt et al., 2014). Therefore, the drainage and imbibition processes carry an important distinction. However, as we showed in Fig. 4c and 7c, the drainage and imbibition capillary pressure curves collapsed into a single curve after using the effective water saturation for the capillary pressure curves. This means the effect of hysteresis i.e., the discrepancy between the drainage and imbibition curves is negligible and confirms the importance of resistance to flow in both cases over long times. Accordingly, we simply used the term "pore size distribution" to estimate the imbibition water relative permeability in this study.

As relative permeability is an integral effect of flow through different pores, its accurate estimation requires precise knowledge of the critical water saturation, S_{wc}. In our approach, S_{wc} is primarily a function of critical pore radius r_c and residual water saturation, S_{wr}. Although the latter may be determined from the capillary pressure

curve, the former is difficult to be measured, particularly for different water saturations. The value of the critical water saturation is not universal and varies from one porous medium to another. It mainly depends on the connectivity of the porous medium. Within the percolation theory framework, one should expect the critical water saturation to decrease as the average coordination number (Z) increases i.e., $S_{wc} \propto \frac{1}{Z}$ (Sahimi, 1993; 2011; Ghanbarian et al., 2015b). In addition, S_{wc} is affected by the scale or sample size. Finite-size scaling theory of Fisher (1971) and Levinshtein et al. (1976) indicated that one should expect a shift in the critical water saturation for the finite size of a pore network. Wetting properties of the pore space also affect the critical water saturation and relative permeability. One should expect the water relative permeability to be higher in a hydrophobic medium than it would be if the medium is hydrophilic (see e.g., Anderson, 1987). Accordingly, the critical water saturation in a hydrophobic medium should be less than that in the same medium under hydrophilic conditions.

Moreover, it is well known in the literature that both flow rate and capillary number influence critical saturation for relative permeability. Experimental observations of Larson et al. (1981), Chatzis and Morrow (1984), Fulcher et al. (1985), among many others showed that critical saturation for relative permeability is roughly constant at low capillary numbers. At some capillary number, however, a knee occurs in the critical saturation-capillary number curve and critical saturation starts to decrease (see Fig. 3.17 in Lake (1989)).

We emphasize that estimating the critical water saturation is complicated, because its value is affected by several factors, such as the pore connectivity, wettability, capillary number, sample size. There are also other factors, the quantification and integrated influence of which within a theoretical framework are challenging problems. Further investigations are then required to study the critical saturation in thin porous media, such as paper coating layers and uncoated papers.

We should also point out that as fibers absorb liquid they may swell and, accordingly, their geometrical and morphological properties are subjected to vary. The effect of swelling on fiber diameter as well as pore structure has been addressed in the literature. For example, Aslannejad and Hassanizadeh (2017) demonstrated that the fiber diameter could increase by 23% after 50 s. Although drying the swelled fiber for 280 s caused reduction in diameter by 15%, their results indicated that the fiber diameter variation is not entirely reversible.

In another study, Lamminmäki et al. (2011) investigated the effect of swelling on ink imbibition in terms of ink penetration and spreading. They showed that small pores play a key role in the ink imbibition process during the first two seconds. Their results indicated that the swelling of fibrous matrix can strongly increase the structural thickness. Further investigation is required to address the dynamic effect of swelling on the water relative permeability during the imbibition process.

6. Conclusion

We developed a theoretical model for estimating the water relative permeability from pore size distribution derived from images. To do so, we combined concepts from critical path analysis (CPA) and the universal power-law scaling of percolation theory. We assumed that the pore size distribution conformed to the log-normal distribution and evaluated our model using two media including a paper coating layer and an uncoated paper. Comparison with pore-scale numerical simulations performed on the real 3D images indicated that CPA provided accurate estimates of water relative permeability at high water saturations. The universal power-law scaling from percolation theory, which accounts for the effect of both the tortuosity and connectivity at low water saturations, provided precise estimates in the region near the critical water saturation, S_{wc}. We showed that the proposed theoretical model can be used to accurately determine fluid ink and/or ink vehicle permeation and spreading inside paper coating layers as well as uncoated papers.

Acknowledgement

BG is grateful to Kansas State University for supports through faculty startup funds. HA would like to thank for supports received from Océ-Technologies B.V. and European Research Council (ERC) under the ERC Grant Agreement No. 341225. The authors are grateful to two anonymous reviewers for their constructive comments.

References

Ambegaokar, V., Halperin, B.I., Langer, J.S., 1971. Hopping conductivity in disordered systems. Phys. Rev. B 4 (8), 2612–2620.
Anderson, W.G., 1987. Wettability literature survey-Part 5: the effects of wettability on relative permeability. J. Petrol. Technol. 39 (11), 1453–1468.
Aslannejad, H., Hassanizadeh, S.M., 2017. Study of hydraulic properties of uncoated paper: image analysis and pore-scale modeling. Transp. Porous Media, 1–15.
Aslannejad, H., Hassanizadeh, S.M., Raoof, A., de Winter, D.A.M., Tomozeiu, N., van Genuchten, M.T., 2017. Characterizing the hydraulic properties of paper coating layer using FIB-SEM tomography and 3D pore-scale modeling. Chem. Eng. Sci. 160, 275–280.
Burdine, N., 1953. Relative permeability calculations from pore size distribution data. J. Petrol. Technol. 5 (03), 71–78.
Chatzis, I., Morrow, N.R., 1984. Correlation of capillary number relationships for sandstone. Soc. Pet. Eng. J. 24 (5), 555–562.
Coates, G.R., Xiao, L., Prammer, M.G., 1999. NMR Logging: Principles and Applications. Haliburton Energy Services, Houston, p. 234.
Delerue, J.F., Perrier, E., Yu, Z.Y., Velde, B., 1999. New algorithms in 3D image analysis and their application to the measurement of a spatialized pore size distribution in soils. Phys. Chem. Earth Part A. 24 (7), 639–644.
Dodson, C.T.J., Sampson, W.W., 1996. The effect of paper formation and grammage on its pore size distribution. J. Pulp Pap. Sci. 22 (5), J165–J169.
Fisher, M.E., 1971. The theory of critical point singularities. In: Green, M.S. (Ed.), Critical Phenomena: Proceedings of the 1970 Enrico Fermi International School of Physics, Varenna, Italy. Course 51. Academic, N.Y., pp. 1–99.
Fulcher Jr., R.A., Ertekin, T., Stahl, C.D., 1985. Effect of capillary number and its constituents on two-phase relative permeability curves. J. Pet. Technol. 37 (02), 249–260.
Ghanbarian-Alavijeh, B., Hunt, A.G., 2012. Unsaturated hydraulic conductivity in porous media: percolation theory. Geoderma 187–188, 77–84.
Ghanbarian, B., Hunt, A.G., 2017. Improving unsaturated hydraulic conductivity estimation in soils via percolation theory. Geoderma 303, 9–18.
Ghanbarian, B., Hunt, A.G., Skinner, T.E., Ewing, R.P., 2015a. Saturation dependence of transport in porous media predicted by percolation and effective medium theories. Fractals 23, 1540004.
Ghanbarian, B., Daigle, H., Hunt, A.G., Ewing, R.P., Sahimi, M., 2015b. Gas and solute diffusion in partially saturated porous media: percolation theory and effective medium approximation compared with lattice Boltzmann simulations. J. Geophys. Res. Solid Earth 120 (1), 182–190.
Ghanbarian, B., Hunt, A.G., Daigle, H., 2016a. Fluid flow in porous media with rough pore-solid interface. Water Resour. Res. 52, 2045–2058.
Ghanbarian, B., Sahimi, M., Daigle, H., 2016b. Modeling relative permeability of water in soil: application of effective-medium approximation and percolation theory. Water Resour. Res. 52 (7), 5025–5040.
Ghanbarian, B., Ioannidis, M.A., Hunt, A.G., 2017. Theoretical insight into the empirical tortuosity-connectivity factor in the Burdine-Brooks-Corey water relative permeability model. Water Resour. Res. 53, 10395–10410. https://doi.org/10.1002/2017WR021753.
Ghassemzadeh, J., Hashemi, M., Sartor, L., Sahimi, M., 2001. Pore network simulation of imbibition into paper during coating: I. Model development. AIChE J. 47, 519–535.
Ghassemzadeh, J., Sahimi, M., 2004a. Pore network simulation of fluid imbibition into paper during coating: II. Characterization of paper's morphology and computation of its effective permeability tensor. Chem. Eng. Sci. 59, 2265–2280.
Ghassemzadeh, J., Sahimi, M., 2004b. Pore network simulation of fluid imbibition into paper during coating—III: modelling of the two-phase flow. Chem. Eng. Sci. 59 (11), 2281–2296.
Huang, S., Goel, A., Ramaswamy, S., Ramarao, B.V., Choi, D., 2002. Transverse and in-plane pore structure characterization of paper. Appita J. 55 (3), 230–234.
Hunt, A.G., 2001. Applications of percolation theory to porous media with distributed local conductances. Adv. Water Resour. 24 (3), 279–307.
Hunt, A.G., Idriss, B., 2009. Percolation-based effective conductivity calculations for bimodal distributions of local conductances. Phil. Mag. 89, 1989–2007.
Hunt, A., Ewing, R., Ghanbarian, B., 2014. Percolation Theory for Flow in Porous Media, Lect. Notes Phys. vol. 880, third ed., Springer, Berlin.

Järnström, J., Väisänen, M., Lehto, R., Jäsberg, A., Timonen, J., Peltonen, J., 2010. Effect of latex on surface structure and wetting of pigment coatings. Colloids Surf. A: Physicochem. Eng. Aspects 353 (2), 104–116.
Kainourgiakis, M.E., Kikkinides, E.S., Stubos, A.K., Kanellopoulos, N.K., 1998. Adsorption–desorption gas relative permeability through mesoporous media—network modelling and percolation theory. Chem. Eng. Sci. 53 (13), 2353–2364.
Katz, A.J., Thompson, A.H., 1986. Quantitative prediction of permeability in porous rock. Phys. Rev. B 34 (11), 8179–8181.
Katz, A.J., Thompson, A.H., 1987. Prediction of rock electrical conductivity from mercury injection measurements. J. Geophys. Res. Solid Earth 92 (B1), 599–607.
Koivula, H., Toivakka, M., Gane, P., 2012. Short time spreading and wetting of offset printing liquids on model calcium carbonate coating structures. J. Colloid Interface Sci. 369, 426–434.
Kosugi, K., 1999. General model for unsaturated hydraulic conductivity for soils with lognormal pore-size distribution. Soil Sci. Soc. Am. J. 63 (2), 270–277.
Lamminmäki, T.T., Kettle, J.P., Gane, P.A.C., 2011. Absorption and adsorption of dye-based inkjet inks by coating layer components and the implications for print quality. Colloids Surf. A Physicochem. Eng. Asp. 380, 79–88.
Lake, L.W., 1989. Enhanced Oil Recovery. Prentice Hall Inc., Old Tappan, NJ, p. 577.
Larson, R.G., Davis, H.T., Scriven, L.E., 1981. Displacement of residual nonwetting fluid from porous media. Chem. Eng. Sci. 36 (1), 75–85.
Levinshtein, M.E., Shklovskii, B.I., Shur, M.S., Efros, A.L., 1976. The relation between the critical exponents of percolation theory. Sov. Phys. JETP Engl. Transl. 42, 197–200.
Lindquist, W.B., Lee, S.M., Coker, D.A., Jones, K.W., Spanne, P., 1996. Medial axis analysis of void structure in three-dimensional tomographic images of porous media. J. Geophys. Res. 101, 8297–8310.
Liu, M., Mostaghimi, P., 2017. High-resolution pore-scale simulation of dissolution in porous media. Chem. Eng. Sci. 161, 360–369.
Liu, G., Zhang, M., Ridgway, C., Gane, P., 2014a. Spontaneous inertial imbibition in porous media using a fractal representation of pore wall rugosity. Transp. Porous Media 104 (1), 231–251.
Liu, G., Zhang, M., Ridgway, C., Gane, P., 2014b. Pore wall rugosity: the role of extended wetting contact line length during spontaneous liquid imbibition in porous media. Colloids Surf. A: Physicochem. Eng. Aspects 443, 286–295.
Liu, G., Fu, S., Lu, Z., Zhang, M., Ridgway, C., Gane, P., 2017. Contrasting liquid imbibition into uncoated versus pigment coated paper enables a description of imbibition into new-generation surface-filled paper. Euro. Phys. J. E 40 (12), 111.
Liukkonen, A., 1997. Contact angle of water on paper components: sessile drops versus environmental scanning electron microscope measurements. Scanning 19 (6), 411–415.
Mualem, Y., 1976. A new model for predicting the hydraulic conductivity of unsaturated porous media. Water Resour. Res. 12 (3), 513–522.
Øren, P.E., Bakke, S., 2003. Reconstruction of Berea sandstone and pore-scale modelling of wettability effects. J. Pet. Sci. Eng. 39, 177–199.
Petropoulos, J.H., Petrou, J.K., Kanellopoulos, N.K., 1989. Explicit relation between relative permeability and structural parameters in stochastic pore networks. Chem. Eng. Sci. 44 (12), 2967–2977.
Pollak, M., 1972. A percolation treatment of dc hopping conduction. J. Non Cryst. Solids 11, 1–24.
Purcell, W.R., 1949. Capillary pressures-their measurement using mercury and the calculation of permeability therefrom. J. Petrol. Technol. 1 (2), 39–48.
Qin, C.Z., Hassanizadeh, S.M., 2014. Multiphase flow through multilayers of thin porous media: general balance equations and constitutive relationships for a solid–gas–liquid three-phase system. Int. J. Heat Mass Transf. 70, 693–708.
Qin, C.Z., Hassanizadeh, S.M., Ebigbo, A., 2016. Pore-scale network modeling of microbially induced calcium carbonate precipitation (MICP): insight into scale dependence of biogeochemical reaction rates. Water Resour. Res. 52, 8794–8810.
Raoof, A., Hassanizadeh, S.M., 2012. A new formulation for pore-network modeling of two-phase flow. Water Resour. Res. 48 (1), W01514.
Raoof, A., Nick, H.M., Hassanizadeh, S.M., Spiers, C.J., 2013. PoreFlow: a complex pore-network model for simulation of reactive transport in variably saturated porous media. Comput. Geosci. 61, 160–174.
Sahimi, M., 1993. Nonlinear transport processes in disordered media. AIChE J. 39 (3), 369–386.
Sahimi, M., 1994. Applications of Percolation Theory. Taylor and Francis, London, p. 258.
Sahimi, M., 2011. Flow and Transport in Porous Media and Fractured Rock. Wiley-VCH, Weinheim.
Silin, D.B., Jin, G., Patzek, T.W., 2003. Robust determination of the pore space morphology in sedimentary rocks, In: Paper SPE 84296 presented at Society of Petroleum Engineers Annual Technical Conference and Exhibition, Denver, CO.
Stauffer, D., Aharony, A., 1994. Introduction to Percolation Theory. Taylor and Francis, London.
Tsakiroglou, C.D., Ioannidis, M.A., 2008. Dual-porosity modelling of the pore structure and transport properties of a contaminated soil. Eur. J. Soil Sci. 59 (4), 744–761.
Wildenschild, D., Sheppard, A.P., 2013. X-ray imaging and analysis techniques for quantifying pore-scale structure and processes in subsurface porous medium systems. Adv. Water Resour. 51, 217–246.
van Genuchten, M.T., 1980. A closed-form equation for predicting the hydraulic conductivity of unsaturated soils. Soil Sci. Soc. Am. J. 44 (5), 892–898.
Zhang, T., Li, X., Sun, Z., Feng, D., Miao, Y., Li, P., Zhang, Z., 2017. An analytical model for relative permeability in water-wet nanoporous media. Chem. Eng. Sci. 174, 1–12.
Zheng, Q., Yu, B., Duan, Y., Fang, Q., 2013. A fractal model for gas slippage factor in porous media in the slip flow regime. Chem. Eng. Sci. 87, 209–215.